Sensors and Materials, Vol. 35, No. 8 (2023) 2909–2932
MYU Tokyo

S & M 3364

A Novel MEMS Actuator Driven with a Low DC Voltage

Jun Mizuno

Ishinomaki Senshu University, 1 Shinmito, Minamisakai, Ishinomaki City, Miyagi 986-8580, Japan

(Received March 31, 2023; accepted July 3, 2023)

Keywords: MEMS, actuator, dc driving voltage, pull-in phenomenon, SOI wafer

In this paper, we propose a novel MEMS actuator that can achieve a relatively large in-plane displacement of 5 μm or more driven with a low dc voltage of 3.3 to 5.0 V to ensure compatibility with integrated circuits and microcontroller unit (MCU) boards. The drive mechanism is based on a comb-shaped electrostatic microactuator. However, in general, the electrostatic type can achieve only a small amount of displacement in spite of a large driving voltage. On the other hand, by vacuum-sealing a device with such an actuator to reduce air resistance and performing ac driving at the resonant frequency of the device, the driving voltage can be considerably reduced. However, in the case of devices that need to be driven with dc voltages, such as RF switches, 2D optical raster scanners, optical switches, and various sensors, displacement is not amplified even if operating in a vacuum environment. Moreover, it would be strongly desirable to control these devices directly using integrated circuits and MCU boards without any external driver boosters or power supplies. In this paper, we demonstrate that a 6 μm in-plane displacement can be achieved with a dc driving voltage of less than 8.0 V by using a pull-in phenomenon and multiple spring-mass systems based on a comb-shaped electrostatic MEMS actuator.

1. Introduction

In recent years, research and development toward the fusion of MEMS and LSI, in other words, heterogeneous integration, has become active.(1–3) Integrating MEMS and LSI is expected to facilitate the control of MEMS devices, as well as achieve miniaturization and higher functionality. As a result, the demand for MEMS is expected to increase further in fields such as internet of things, artificial intelligence, robots, and autonomous driving.(4) Developments in these fields have been made possible by research on devices such as accelerometers, angular velocity sensors, pressure sensors, micromirrors, microcantilevers, RF switches, and micro–total analysis systems.(4) On the other hand, as a step before the heterogeneous integration, these devices must be operated at low voltages. However, the MEMS actuator part, which is the device's heart, still remains important in relation to the trade-of between driving voltage and displacement. Usually, these devices are controlled by integrated circuits or microcontroller unit (MCU) boards that operate at dc voltages of 3.3 to 5.0 V.(5) The problem is that if one wants to

*Corresponding author: e-mail: mizuro@isenshu-u.ac.jp
https://doi.org/10.18494/SAM4411

ISSN 0914-4935 © MYU K.K.
https://myukk.org/

operate a microactuator directly using these controllers, only a small amount of displacement on the order of submicron can be attained. To solve this problem, usually, an external insulated gate bipolar transistor (IGBT) or MOSFET gate driver boosters[6–9] combined with high-voltage power supplies are used. However, such additional apparatuses will increase the amount of space required, which will lead to a system enlargement problem. Another method of realizing a large amount of displacement is to vacuum-seal a device to reduce air resistance and to perform an ac drive at the resonance frequency point. Under these conditions, the displacement can be amplified and the voltage can be markedly reduced.[10–13] However, in the case of devices that need to be driven with dc voltages, such as RF switches, 2D optical raster scanners, optical switches, and various sensors, displacement is not amplified even if operating in a vacuum environment. Moreover, it would be strongly desirable to control these devices directly using integrated circuits and MCU boards without any external driver boosters or power supplies. Therefore, if one can make actuators that operate at low dc voltages of 3.3 to 5.0 V, compatibility with integrated circuits and MCU boards can be achieved. When considering the electronic design, we must select among electrostatic, piezoelectric, and electromagnetic drive methods. In this work, we have chosen the electrostatic drive method, because in comparison with the other two drive methods, no electric current flows and only the voltage need be considered. This drive method is very suitable when MCU boards are used for controlling an electrostatic microactuator, because no current is required. In addition, a single general-purpose input/output (GPIO) pin of MCU boards can provide only a maximum current of 16 to 40 mA. These small levels of current are not enough to drive actuators based on either piezoelectric or electromagnetic drive methods. On the other hand, the drawback of the electrostatic drive method is the low capacitance that leads to a small electrostatic force and, consequently, only a small amount of displacement is possible.

Several studies have been conducted over two decades to solve this problem, [14–23] however none of them has achieved a displacement larger than 6 μm at a dc driving voltage typically used in MCU boards. We have focused on this matter and proposed a revolutionary structure that overthrows the conventional structures of electrostatic microactuators, which were considered to be unable to drive large amounts of displacement. In this study, we have demonstrated that a large in-plane displacement can be achieved with a low dc driving voltage by combining a pull-in phenomenon with multiple spring-mass systems based on a comb-shaped electrostatic MEMS actuator.

2. Materials and Methods

In this work, we aim to realize a MEMS actuator that can achieve a relatively large displacement of 5 μm or more by using a low dc operating voltage of 3.3 to 5.0 V. In the following subsections, we describe the theoretical model, concept of device structure, design, and fabrication process.

2.1 Theoretical model

Figure 1(a) shows a typical comb drive actuator, which consists of interdigitated comb teeth. A voltage V is applied to the fixed comb electrode, whereas the movable comb electrode is grounded. Then, the tangential (y-direction) and normal (x-direction) components of the capacitances for a single movable comb tooth, which is surrounded by two fixed comb teeth, can be expressed as

$$C_T(y) = C_{T1}(y) + C_{T2}(y) = 2\varepsilon_r\varepsilon_0\left[\frac{(l-g_T+y)h}{g_R} + \frac{(l-g_T+y)}{g_L} + \frac{hw}{g_T-y}\right], \tag{1}$$

$$C_{NR}(x) = \frac{\varepsilon_r\varepsilon_0(l-g_T)h}{g_R-x}, \tag{2}$$

$$C_{NL}(x) = \frac{\varepsilon_r\varepsilon_0(l-g_T)h}{g_L+x}, \tag{3}$$

where ε_0 (= 8.7754 × 10^{-12} F/m) and ε_r (= 1) are the permittivity of a vacuum and the relative permittivity of the medium, respectively, h is the depth of the comb tooth, w, l, and h are the width, length, and thickness of the comb tooth, g_T is the initial gap between the fixed and movable comb tooth tip, and g_R and g_L are the initial gaps between the side walls of the fixed and movable comb teeth, respectively. The perpendicular capacitances $C_{T1}(y)$ and $C_{T2}(y)$ are equal as the overlapping areas, gaps, and displacements in the y-direction are the same. Since the normal capacitances $C_{NR}(x)$ and $C_{NL}(x)$ are on opposite sides, the sign of the displacement x is also opposite. Therefore, based on the coordinates shown in Fig. 1(a), the denominators of the fractions for $C_{NR}(x)$ and $C_{NL}(x)$ in Eqs. (2) and (3) are $g_R - x$ and $g_L + x$, respectively.

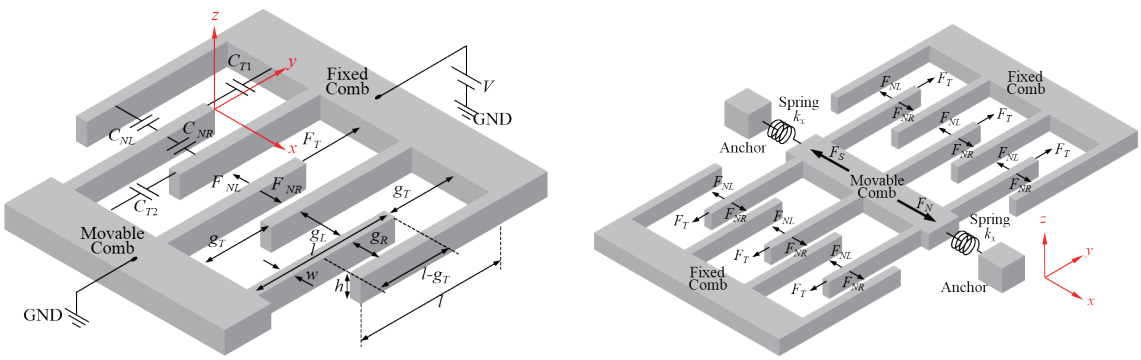

(a) (b)

Fig. 1. (Color online) Schematic of comb drive actuator: (a) illustration of the capacitances, electrostatic forces and structure dimensional parameters and (b) movable comb suspended by springs.

From Eqs. (1)–(3) the tangential and normal electrostatic forces acting on the movable comb tooth are

$$F_T(y) = \frac{1}{2}\frac{\partial C_T(y)}{\partial y}V^2 = \varepsilon_r\varepsilon_0 hV^2\left[\frac{1}{g_R} + \frac{1}{g_L} + \frac{w}{(g_T - y)^2}\right], \tag{4}$$

$$F_{NR}(x) = \frac{1}{2}\frac{\partial C_{NR}(x)}{\partial x}V^2 = \frac{1}{2}\frac{\varepsilon_r\varepsilon_0(l - g_T)h}{(g_R - x)^2}V^2, \tag{5}$$

$$F_{NL}(x) = \frac{1}{2}\frac{\partial C_{NL}(x)}{\partial x}V^2 = -\frac{1}{2}\frac{\varepsilon_r\varepsilon_0(l - g_T)h}{(g_L + x)^2}V^2. \tag{6}$$

Figure 1(b) shows the extended model of Fig. 1(a). Teeth are symmetrically placed on the movable comb along the x-direction, which are interdigitated with the teeth of the fixed comb. The resultant tangential force acting on the movable comb is always zero because of the force balance condition. On the other hand, the resultant normal force acting on the movable comb teeth is

$$F_N(x) = n_R F_{NR}(x) + n_L F_{NL}(x) = \frac{1}{2}\varepsilon_r\varepsilon_0(l - g_T)hV^2\left[\frac{n_R}{(g_R - x)^2} - \frac{n_L}{(g_L + x)^2}\right], \tag{7}$$

where n_R and n_L are the number of comb teeth that generate forces $F_{NR}(x)$ and $F_{NL}(x)$, respectively.

The movable comb is suspended by springs on both side ends. In addition, the opposite side of each spring is anchored (fixed). A single spring has a spring constant of k_x. The movable comb is suspended by two springs that have the same spring constant. Thus, the equivalent spring constant is

$$k_{eq} = 2k_x, \tag{8}$$

and when the movable comb is displaced by the amount x, the spring restoring force is

$$F_S(x) = -k_{eq}x = -2k_x x. \tag{9}$$

Hereinafter, the movable comb is named the proof mass. From Eqs. (7) and (9), the resultant force acting on the proof mass is

$$F_{res}(x) = F_N(x) + F_S(x) = \frac{1}{2}\varepsilon_r\varepsilon_0(l - g_T)hV^2\left[\frac{n_R}{(g_R - x)^2} - \frac{n_L}{(g_L + x)^2}\right] - 2k_x x . \quad (10)$$

For a displacement x, the resultant force acting on the movable comb satisfies the following force balance condition,

$$F_{res}(x) = F_N(x) + F_S(x) = 0 , \quad (11)$$

and from Eqs. (10) and (11), we obtain the following force balance equation:

$$\frac{1}{2}\varepsilon_r\varepsilon_0(l - g_T)hV^2\left[\frac{n_R}{(g_R - x)^2} - \frac{n_L}{(g_L + x)^2}\right] - 2k_x x = 0 . \quad (12)$$

From Eq. (12), the relation between voltage V and displacement x is

$$V = 2(g_R - x)(g_L + x)\sqrt{\frac{k_x x}{\varepsilon_r\varepsilon_0(l - g_T)h\left[n_R(g_L + x)^2 - n_L(g_R - x)^2\right]}} . \quad (13)$$

Hereinafter, the values for the variables are basically taken from Table 2 in Sect. 2.3. However, for some variables, the design values and the actual fabricated dimensions are slightly different depending on the pattern. In particular, the spring width becomes thinner than the designed value, and the opposite happens for the gaps g_R and g_L. In any case, these parameters become thinner or thicker by about a half-width of 250 nm based on fabrication process experience [in the case of the following device fabrication process: chromium photomask (laser drawing followed by wet etching), patterning by photolithography, and deep-reactive ion etching]. For these variables, the half-width change values have been considered for the calculation.

From Eqs. (7) and (9), we have plotted the electrostatic force $F_N(x)$ (for V = 4.0 V) and the storing force $-F_S(x)$ (storing force) as functions of displacement x, respectively, as shown in Fig. 2(a). The electrostatic force has a nonlinear characteristic with respect to the displacement x and it is a reciprocal squared function. On the other hand, the storing force is a linear function. The electrostatic force intersects the spring restoring force at points A and B, as shown in Fig. 2(a). These two points, which satisfy the force balance condition, are the solution for the Eq. (11). Next, we discuss the stability of the actuator system. When a voltage is applied, the proof mass starts to move in the positive direction of the x-axis, since the electrostatic force is larger than the spring restoring force and stops at point A, since the force balance condition is satisfied. Any slight perturbation in one direction or the other will not allow the system to diverge (i.e., the proof mass will not be pulled towards the fixed comb). Thus, the proof mass will always return to point A, which means that at this point, the system is stable. Let us now consider the system

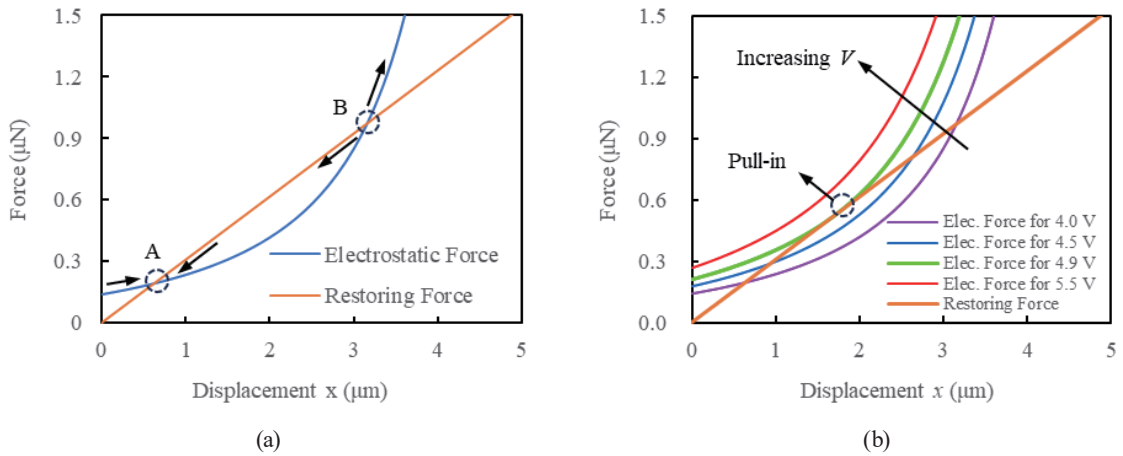

Fig. 2. (Color online) Electrostatic and spring restoring force relations as functions of displacement: (a) for a voltage $V = 4.0$ V and (b) for voltages of 4.0, 4.5, 4.9, and 5.5 V.

stability at point B: 1) if a slight perturbation moves the proof mass to the negative direction of the x-axis, the spring restoring force will be larger than the electrostatic force. The relation of these two forces will be kept up to point A. Thus, the proof mass moves back further until it reaches the point A; 2) if a slight perturbation moves the proof mass to the positive direction of the x-axis, the electrostatic force will always be larger than the spring restoring force. Thus, the proof mass will move forward until it contacts the fixed comb, which means that at this point, the system is unstable.

The system stability needs to be further investigated to understand the actuator operation under the pull-in condition. We have calculated the electrostatic and spring restoring forces for various driving voltages. Four curves for different driving voltages have been plotted, as shown in Fig. 2(b). As the driving voltage increases, the curves move towards the restoring force curve. For voltages of 4.0 and 4.5 V, the curves intersects the restoring force at two points, similar to Fig. 2(a). On the other hand, for a voltage of 4.9 V, the curve intersects the restoring force at only one point. At this point, the equilibrium state is at the stability threshold. This is a critical point because when a slight perturbation in one direction or the other occurs, the electrostatic force will always be larger than the restoring force. Thus, the proof mass will be pulled towards the fixed comb until it comes into contact with the fixed comb teeth. This is called the pull-in phenomenon and the voltage $V_{pull\text{-}in}$ is named the pull-in voltage. In this study, the displacement $x_{pull\text{-}in}$, where the pull-in effect starts, is named the pull-in distance. For voltages larger than $V_{pull\text{-}in}$, such as the voltage of 5.5 V, there is no intersection point between the electrostatic and restoring force curves, and the proof mass will always come into contact with the fixed comb teeth. Thus, the system is unstable for voltages larger than $V_{pull\text{-}in}$. Let us examine the equations for the pull-in effect. First, Eq. (11) must be satisfied as the electrostatic and restoring forces intersect at one point. Let us rewrite Eq. (11) as follows.

$$F_N(x) = -F_S(x) \tag{14}$$

Second, the restoring force curve is the tangent line of the electrostatic force curve at the intersection point. To find the tangent line of the electrostatic force, $F_N(x)$ must be partially differentiated with respect to x. At the intersection point, the slopes of the tangent line of the electrostatic and restoring forces are equal. Since the slope of the restoring force curve is also the partial derivative of $F_S(x)$, both sides of Eq. (14) can be partially differentiated and rearranging the terms, we obtain

$$\frac{\partial F_N(x)}{\partial x} = -\frac{\partial F_S(x)}{\partial x} \Rightarrow \frac{\partial F_N(x)}{\partial x} + \frac{\partial F_S(x)}{\partial x} = 0 \Rightarrow \frac{\partial\left[F_N(x) + \partial F_S(x)\right]}{\partial x} = 0\,, \tag{15}$$

and the sum of the terms inside of brackets is the resultant force. Thus, under the pull-in condition, the following equation is satisfied.

$$\frac{\partial F_{res}(x)}{\partial x} = 0 \Rightarrow \varepsilon_r \varepsilon_0 (l - g_T) h V^2 \left[\frac{n_R}{(g_R - x)^3} + \frac{n_L}{(g_L + x)^3}\right] - 2k_x = 0 \tag{16}$$

From Eqs. (12) and (16), we obtain the pull-in distance $x_{pull\text{-}in}$ as follows.

$$x_{pull-in} = \frac{\left(g_R - x_{pull-in}\right)\left(g_L + x_{pull-in}\right)\left[n_R\left(g_L + x_{pull-in}\right)^2 - n_L\left(g_R - x_{pull-in}\right)^2\right]}{2\left[n_R\left(g_L + x_{pull-in}\right)^3 + n_L\left(g_R - x_{pull-in}\right)^3\right]} \tag{17}$$

Equation (17) must be solved using the iteration method. Table 1 shows the solution for Eq. (17). For the first iteration step $n = 0$, we arbitrarily choose the initial value $x_0 = 0$ μm. x_0 is substituted into the iteration formula to obtain the next value. This value is then used for the next substitution, and so on. Table 1 shows the iteration method, indicating the calculation flow with arrows.

Only 12 iterations are needed to converge the value to the fifth decimal place (although the internal calculation is much more precise and it uses 15 digits). Rounding off the value of 1.70853 to two decimal places, we obtain $x_{pull\text{-}in} = 1.71$ μm.

Substituting x by $x_{pull\text{-}in}$ in Eq. (16), the pull-in voltage $V_{pull\text{-}in}$ is

$$V_{pull-in} = \sqrt{\frac{2k_x\left(g_R - x_{pull-in}\right)^3\left(g_L - x_{pull-in}\right)^3}{\varepsilon_r \varepsilon_0 (l - g_T) h\left[n_R\left(g_L + x_{pull-in}\right)^3 + n_L\left(g_R - x_{pull-in}\right)^3\right]}}\,, \tag{18}$$

and we obtain a value of $V_{pull\text{-}in} = 4.89$ V.

Table 1
(Color online) Iteration method to solve Eq. (17).

Iteration Step	Initial or New Value	Iteration Formula
n	x_n (μm)	$x_{n+1} = \dfrac{(g_R - x_n)(g_L + x_n)\left[n_R(g_L + x_n)^2 - n_L(g_R - x_n)^2\right]}{2\left[n_R(g_L + x_n)^3 + n_L(g_R - x_n)^3\right]}$ (μm)
0	0	1.92504
1	1.92504	1.63789
2	1.63789	1.73007
3	1.73007	1.70181
4	1.70181	1.71061
5	1.71061	1.70788
6	1.70788	1.70873
7	1.70873	1.70846
8	1.70846	1.70855
9	1.70855	1.70852
10	1.70852	1.70853
11	1.70853	1.70853

Based on pull-in values for $x_{pull\text{-}in}$ and $V_{pull\text{-}in}$ as well as Eq. (13), the displacement as a function of driving voltage can be plotted as shown in Fig. 3. This graph consists of three equilibrium states: stable, stability threshold, and unstable equilibria. In the stable equilibrium, Eq. (13) holds for $0 \le x < x_{pull\text{-}in}$ and $0 \le V < V_{pull\text{-}in}$. In the stability threshold, Eqs. (17) and (18) hold for $x = x_{pull\text{-}in}$ and $V = V_{pull\text{-}in}$. Finally, in the unstable equilibrium, where $x > x_{pull\text{-}in}$ and $V > V_{pull\text{-}in}$, a sudden rise in displacement occurs and the proof mass comes into contact with the fixed electrodes.

In this study, the actuator is an extended model in comparison to the traditional parallel-plate actuator. If we suppose that $n_R = n_L = 1$ and $(g_L + x) >> (g_R - x)$, the model becomes a simple parallel-plate actuator, and Eqs. (17) and (18) are simplified as

$$x_{pull-in} = \frac{1}{3} g_R, \tag{19}$$

$$V_{pull-in} = \sqrt{\frac{8k_{eq} g_R}{27\varepsilon_r \varepsilon_0 A}}, \tag{20}$$

where the overlap area A is given by $A = (l - g_T)h$. Equations (19) and (20) are identical to those presented in several reports such as Refs. 24 and 25. Thus, one can say that the theoretical results of this study are both rigorous and self-consistent.

Finally, we theoretically discuss the spring constant k_x. The springs illustrated in Fig. 1(b) are just conceptual diagrams. A drawing close to the actual actuator design is shown in Fig. 4(a). In this figure, the spiral springs in Fig. 1(b) have been replaced by folded beams. From their shape, they are named serpentine (snake) springs. The analytical formula of the spring constant for the serpentine spring is given by[26]

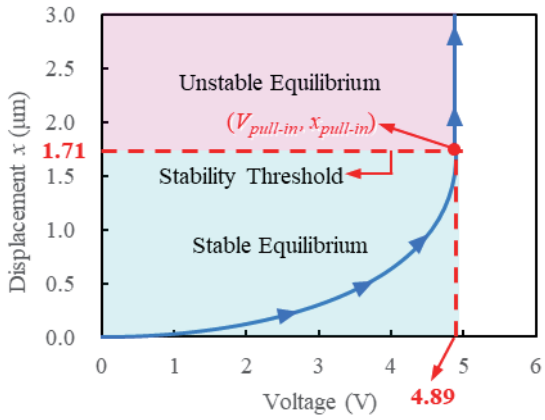

Fig. 3. (Color online) Displacement as a function of driving voltage.

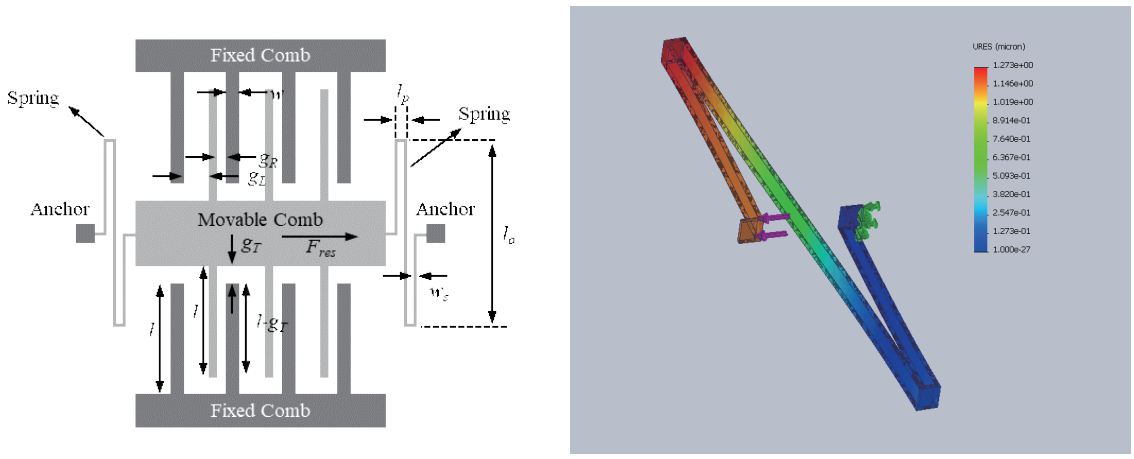

(a) (b)

Fig. 4. (Color online) Schematic closer to actual design: (a) movable comb (proof mass) suspended by serpentine springs and (b) FEA simulation result of a serpentine spring.

$$k_x = \left[\frac{(N+1)l_o^3}{6EI_{zo}} + \frac{(N+1)l_o^2 l_p}{2EI_{zp}} \right], \tag{21}$$

where l_o and l_p are the lengths for the orthogonal and parallel beams in relation to the x-axis, respectively, E is Young's modulus of the structural material, I_{zo} and I_{zp} are the moments of inertial of beams having the lengths of l_o and l_p, respectively, and N is the number of folded turns. Based on Eq. (21), we calculated analytically the spring constant designed for this study and we obtained the following equation:

$$k_x = \frac{Et}{2}\left(\frac{w_s}{l_o}\right)^3\left(1+3\frac{l_p}{l_o}\right)^{-1}, \tag{22}$$

where t and w_s are the thickness and width of the spring, respectively.

In order to verify Eq. (22), finite element analysis (FEA) has been performed using SolidWorks Simulation®, as shown in Fig. 4(b). The spring constant as a function of spring width obtained by analytical and FEA simulation results are shown in Fig. 5. Since the relative error is within 5%, one can say that the analytical equation is self-consistent.

2.2 Structure concept

Figure 6(a) shows the top view of the schematic for the proposed structure. To precisely explain the concept, we use the words "top, bottom, left, and right", which refer to the orientation relative to the in-plane of the drawn structure. The whole structure consists of a single silicon (Si) semiconductor layer. Three proof masses [proof mass 1 to proof mass 3, as shown in Fig. 6(a)] are linked to each other by springs, and the springs linked to the left and right ends of proof masses 1 and 3, respectively, are connected to fixed ends. One comb tooth [named the movable comb tooth, as shown in Fig. 6(a)] comes out from the top and bottom sides of each proof mass. A fixed electrode structure is placed on the top and bottom sides of each proof mass. Two comb teeth [named fixed comb teeth, as shown in Fig. 6(a)] come out from each fixed electrode. Therefore, comb-teeth-type electrostatic electrodes are used, where one side is fixed (i.e., fixed electrode) and the other side, which is connected to the proof mass supported by springs, is movable (i.e., movable electrode). The originality and innovation of this structure lie in the following three points. First point: when a potential difference is applied to the comb teeth facing each other, a Coulomb force (electrostatic force F_N) is generated perpendicularly to the teeth sidewalls, and they are attracted to each other like flat plate electrodes. Therefore, by intentionally causing the pull-in phenomenon, which should never occur in an electrostatic

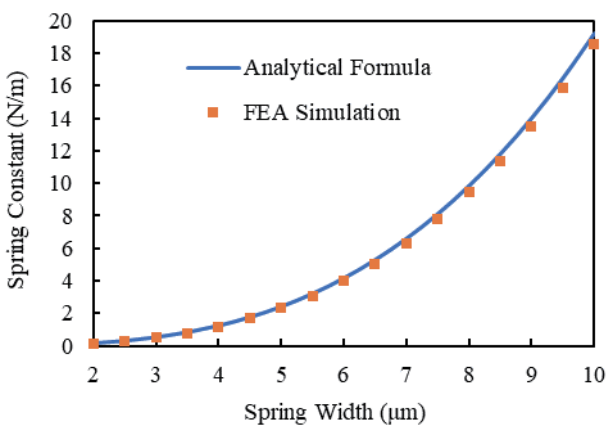

Fig. 5. (Color online) Analytical and FEA simulation results for spring constant as a function of spring width.

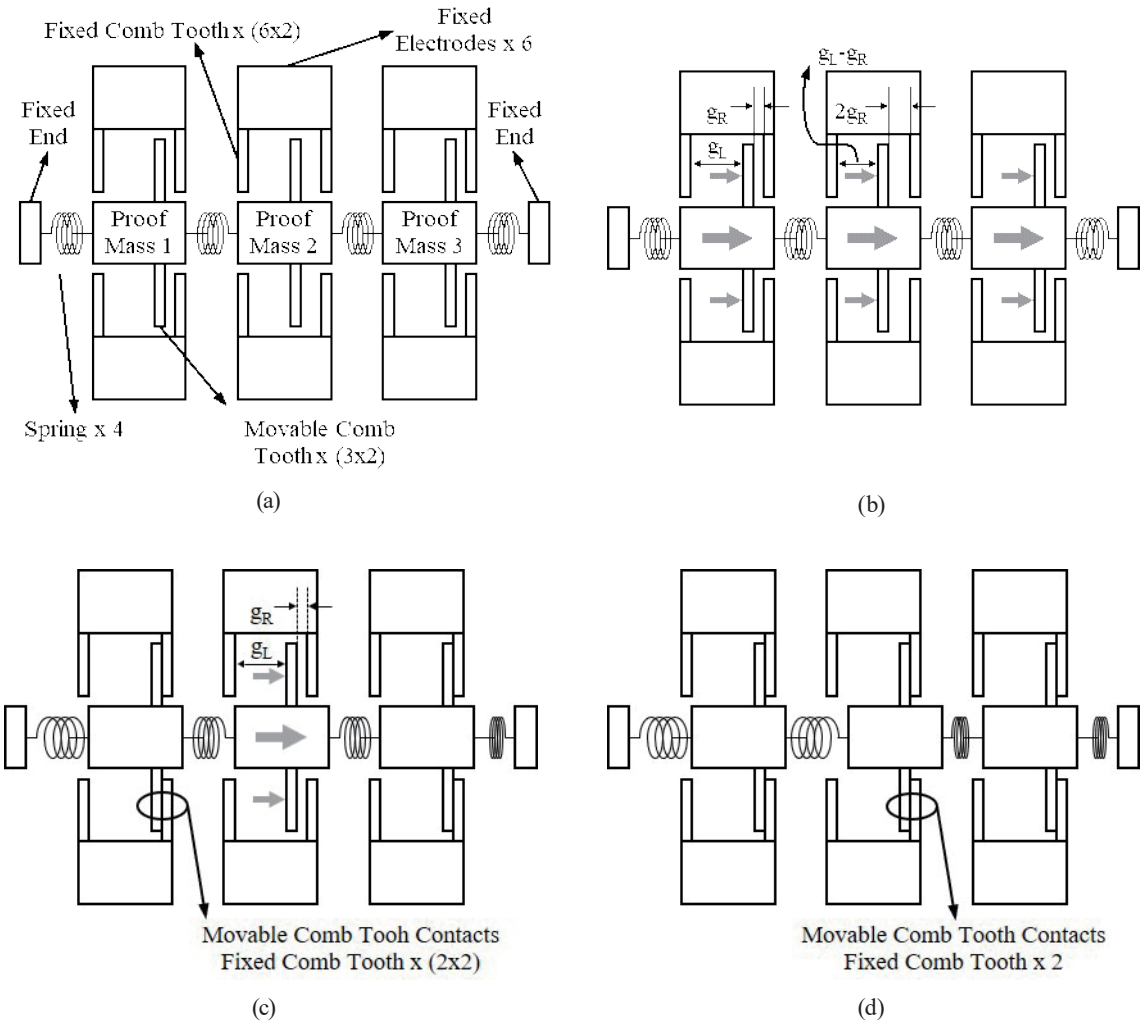

Fig. 6. (Color online) Schematic of proposed structure: (a) names of parts, (b) moving direction, (c) first pull-in, and (d) second pull-in.

actuator, the voltage can be lowered. As explained above, pull-in is a phenomenon in which the electrostatic force becomes larger than the restoring force of the spring at a certain voltage, and the movable electrode suddenly sticks to the fixed electrode. The voltage at which pull-in occurs is called the pull-in voltage. Therefore, the pull-in phenomenon is considered to be an effective means of lowering the driving voltage by adjusting the comb teeth gap (i.e., distance between adjacent comb teeth) and the spring constant. Moreover, it is possible to further reduce the pull-in voltage by increasing the number of comb teeth and the thickness of the comb teeth in the vertical direction. Second point: when the electrodes come into contact with each other as described above, an electrical short circuit occurs, causing the actuator to malfunction. To avoid this problem, it is necessary to limit the current by connecting a high resistance to the power supply side (e.g., general-purpose resistors with resistance values on the order of 10 to 100 MΩ). In addition, permanent sticking can be prevented by reducing the contact area. Specifically,

protrusions of about 2 μm are formed in the longitudinal direction of the comb teeth. Third point: in the conventional structure, it is common to provide a spring structure on both sides of the structure that supports the movable electrode, but this structure cannot be driven at a low voltage. In the proposed structure, the pull-in phenomenon occurs several times over multiple stages with multiple spring-mass systems. Therefore, the amount of maximum displacement required is obtained by multiplying a single spring-mass system displacement set to the pull-in gap by the number of times the pull-in phenomenon occurs. As mentioned above, based on the pull-in phenomenon and subsequent sticking problem countermeasure and the multiple spring-mass systems mechanism, we are able to explain what happens to the proposed structure as follows. When a voltage is applied to the fixed electrodes, electrostatic forces (illustrated as small arrows on each movable comb tooth) are perpendicularly generated on the movable comb teeth side walls, and the three proof masses, which are continuously grounded, move toward the right, as shown in Fig. 6(b). On the other hand, an opposite force works on the same movable teeth. To eliminate the effect of such an undesirable force, gap g_L is adjusted to be much larger than gap g_R. Since gap g_R is set to a distance corresponding to the voltage at which the pull-in phenomenon occurs, when the voltage reaches this value, the three proof masses move a distance equal to gap g_R. At this moment, the movable comb teeth of proof masses 1 and 3 come into contact with the fixed comb tooth, as shown in Fig. 6(c). At the same time, proof mass 2 also moves a distance equal to gap g_R, because of the same amount of movement of proof masses 1 and 3, as shown in Fig. 6(c). Moreover, both spring ends of proof mass 2 have exactly the same displacement g_R; thus, they neither contract nor expand. At this moment, the gap between the fixed and movable comb teeth of proof mass 2 is g_R, as shown in Fig. 6(c). Since gap g_R is set to a distance corresponding to the voltage at which the pull-in phenomenon occurs, as mentioned above, and the voltage is still maintained at the pull-in voltage, proof mass 2 moves a distance equal to gap g_R toward the right. Finally, the movable comb tooth of proof mass 2 comes into contact with the fixed comb tooth, as shown in Fig. 6(d). Therefore, in this structure, the total displacement of proof mass 2 is $2g_R$.

2.3 Design method

To understand the structure concept, we mentioned that the whole structure consists of a single Si layer. Obviously, this is true; however, to explain the design method, we need to specify the original material. A silicon-on-insulator (SOI) wafer has been used. This wafer consists of three layers: a Si layer (named the device layer), a silicon dioxide (SiO_2) insulating layer (named the box layer), and a supporting Si layer (named the handle layer). The structure mentioned in the previous subsection consists of this device layer.

The structure design is similar to that of the concept, as shown in Fig. 7(a). Hereinafter, proof masses 1 and 3 are named the external proof masses, and proof mass 2 is named the center proof mass. Two types of actuator, labeled “design type-1” and “design type-2”, with different comb tooth gaps have been designed. Three actuators have been arranged in a row for each design (i.e., 3 actuators × 2 types, totaling six actuators). They have been designed on a 20 mm square SOI wafer (thicknesses of device layer: 20 μm, box layer: 2 μm, handle layer: approximately 525

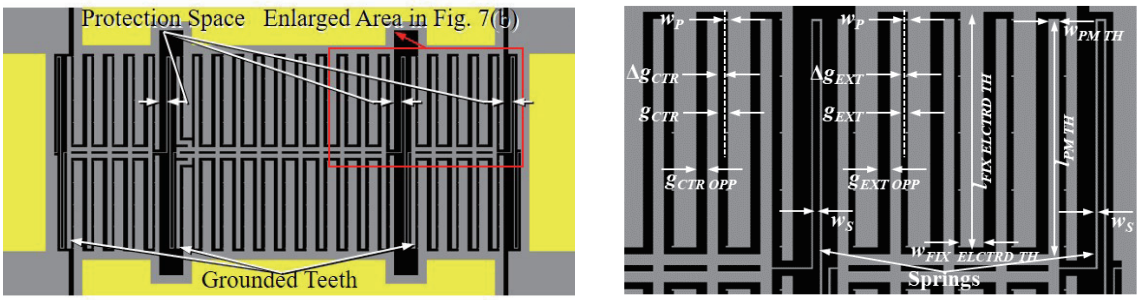

(a) (b)

Fig. 7. (Color online) Actuator design: (a) actuator part and (b) enlarged area for visualization of design variables.

μm). Hereinafter, the values in brackets are for design type-2. The design consists of three proof masses linked by serpentine springs with a width of w_S = 2.5 μm. The external and center proof masses have four and 10 rectangular through holes, respectively. The sizes of these through holes have been designed to lead to a proof mass having a ladder-frame-like structure with a width of 10 μm. The reason for having such through holes is explained in the fabrication method subsection. Five comb teeth, with dimensions of width $w_{PM\ TH}$ = 10 μm and length $l_{PM\ TH}$ = 200 μm, come out from the external proof masses. On the other hand, for the center proof mass, eleven comb teeth come out with the same dimensions as that of the external one. From the fixed electrode, comb teeth with dimensions of width $w_{FIX\ ELCTRD\ TH}$ = 20 μm and length $l_{FIX\ ELCTRD\ TH}$ = 200 μm come out, and they are interdigitated with the comb teeth that come out from the proof mass. The gap between the interdigitated comb teeth is g_{EXT} = 5 μm (10 μm) and g_{CTR} = 8 μm (18 μm) for the external and center proof masses, respectively. However, a protrusion of w_P = 2 μm is formed in the longitudinal direction of the electrode comb teeth (five for each teeth), as explained in the previous subsection. Thus, when a driving voltage is applied to the electrodes, the proof mass moves minus 2 μm from the gap value, which leads to effective displacements of Δg_{EXT} = 3 μm (8 μm) and Δg_{CTR} = 6 μm (16 μm) for the external and center proof masses, respectively. The gaps of the opposite side where the comb teeth are separating from each other during the displacement are g_{EXTL_OPP} = 10 μm (15 μm) and g_{CTR_OPP} = 8 μm (18 μm) for the external and center proof masses, respectively. The designed parameters mentioned above are illustrated in the enlarged area shown in Fig. 7(b). Table 2 summarizes the values for these parameters, which are used for the photomask design.

Another important point in designing the structure is to completely isolate the grounded parts from the applied driving voltage parts. The springs are electrically very sensitive due to their low stiffness. In this design, the comb teeth adjacent to the springs, named "grounded teeth", are grounded for electrical protection against the fixed electrode teeth, as indicated in Fig. 7(a). Moreover, the folded part of the springs is more widely spaced in relation to the fixed electrode walls in comparison with that of other movable comb teeth. This additional space, named the "protection space", is indicated in Fig. 7(a).

Figure 8(a) shows the entire device. The trench structure, illustrated as black lines (color online), has been designed to provide electrical insulation for each part of the structure. The

Table 2
Parameter dimensions for the designed actuators.

Variables	Design type-1 (μm)	Design type-2 (μm)
Spring width w_S	2.5	2.5
Fixed comb teeth width $w_{FIX\ ELCTRD\ TH}$	20	20
Fixed comb teeth length $l_{FIX\ ELCTRD\ TH}$	200	200
Proof mass comb teeth width $w_{PM\ TH}$	10	10
Proof mass comb length $l_{FIX\ ELCTRD\ TH}$	200	200
Comb gap (external proof mass) g_{EXT}	5	10
Comb gap (center proof mass) g_{CTR}	8	18
Opposite side gap (external proof mass) $g_{EXT\ OPP}$	10	15
Opposite side gap (center proof mass) $g_{CTR\ OPP}$	8	18
Effective displacement (external proof mass) Δg_{EXT}	3	8
Effective displacement (center proof mass) Δg_{CTR}	6	16

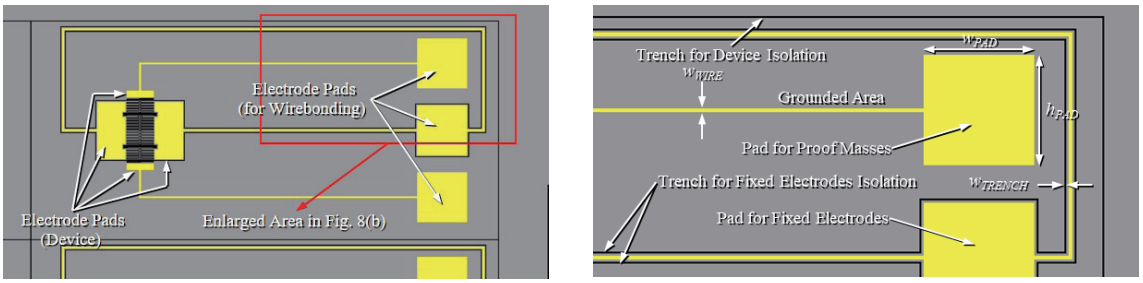

(a) (b)

Fig. 8. (Color online) Device design: (a) entire device and (b) enlarged area for detailed visualization of wiring and trench structures.

depth of the trench structure is d_{DEPTH} = 20 μm, which is the same as the thickness of the device layer, and the width is w_{TRENCH} = 10 μm. Each device is surrounded by a trench to electrically separate each other. Basically, almost the entire device is grounded for the movable structure, except for the electrode part. Therefore, this part must be electrically isolated from the rest of the grounded part by a trench structure. The yellow part (color online) in Fig. 8(a) indicates aluminum-1 wt% silicon alloy (Al-1 wt% Si) material, which has been sputtered on the surface of the device layer. A wire with w_{WIRE} = 5 μm connects the electrode pads located near the device to square electrode pads with the dimensions of width w_{PAD} = 800 μm and length h_{PAD} = 800 μm. The electrode pad in the middle is for applying driving voltage to the fixed electrodes, and the remaining two pads are for grounding the moving proof masses. The designed parameters mentioned above are illustrated in the enlarged area shown in Fig. 8(b). Table 3 shows the values for theses parameters. A wire bonder has been used to connect these electrode pads to the bonding pads of the ceramic package.

2.4 Fabrication method

As mentioned in the previous subsection, the devices have been fabricated on a 20 × 20 mm^2 square SOI wafer (thicknesses of device layer: 20 μm, box layer: 2 μm, handle layer: 525 μm). Figure 9 shows the fabrication method from steps (a) to (e) as follows. Step (a): the starting

Table 3
Parameters dimensions for the designed wiring and trench structures.

Variables	Values (μm)
Wire width w_{WIRE}	25
Trench depth d_{TRENCH}	20
Trench width w_{TRENCH}	10
Electrode pad width w_{PAD}	800
Electrode pad height h_{PAD}	800

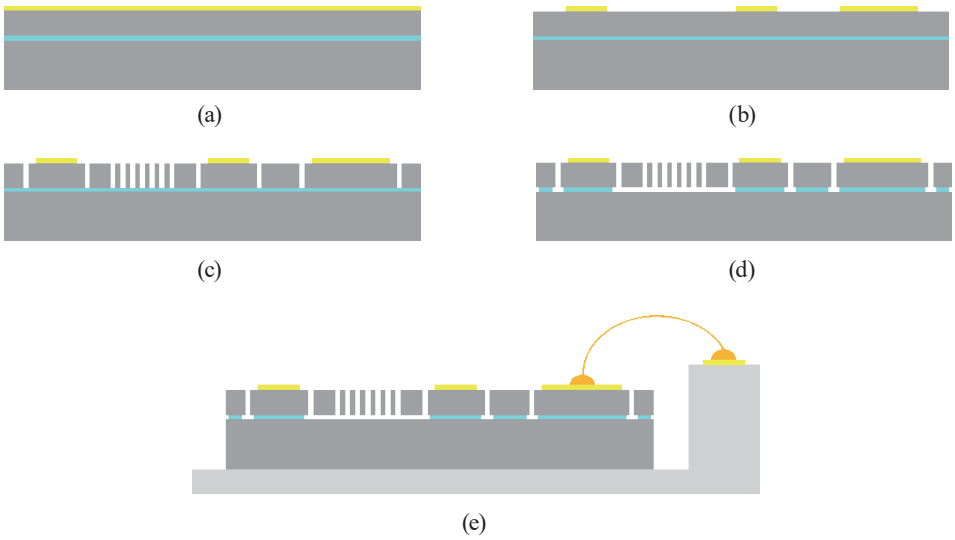

Fig. 9. (Color online) Fabrication process: (a) Al-1 wt% Si sputtering, (b) metal patterning, (c) deep-RIE, (d) vapor HF etching and device release, and (e) die bonding, wire bonding, and glass lid covering (packaging).

material is a 4-in. SOI wafer that has been first sputtered (heating-type sputtering, Shibaura) with an Al-1 wt% Si alloy for the electrode wiring and bonding pads. Step (b): the wafer has been diced (DAD522, Disco) into a 20 mm square wafer chip (illustration omitted). The electrode wiring and bonding pads have been patterned. Step (c): the device and trench structures have been patterned and etched by deep-reactive ion etching (deep-RIE, MUC-21 ASE-SRE, Sumitomo Precision Products). In this process, careful etching must be conducted. A low-scallop (wavy wall shape) etching condition and notching-free process recipe (notching is abnormal erosion etching that occurs near the insulating layer, particularly in narrow trenches) using a low-frequency power supply have been adopted. In particular, low scalloping is essential for the spring walls as they are constantly deformed. If the scallops are relatively large, cracks are likely to occur and the springs will break. Step (d): the box layer is etched using vapor hydrofluoric acid (HF) equipment (μEtch Module TO-α, Sumitomo Precision Products Primaxx). The vapor HF etching is one the key processes because sticking problems can be avoided,[27] particularly for box layers with thickness on the order of two microns. Sticking always occurs when using the widespread method of liquid HF etching. The reason for making rectangular through holes is to enable the complete intrusion of HF gas underneath a wide structure. In this step, the movable

structure is completely released. Step (e): the chip is die bonded on a ceramic package. Then electrode pads of the chip are wire bonded to that of the package. Finally, the package is covered by a glass lid (illustration omitted).

3. Results and Discussion

A SEM (S3700N, Hitachi High Technologies) image of a fabricated device is shown in Fig. 10(a) and 10(b). Figure 10(c) shows the detailed SEM image of the interdigitated comb fingers, and Fig. 10(d) shows a 65 μm width mesa structure where a 25 μm wire is sputtered. In the same figure, two trench structures with a width of 10 μm electrically isolates the mesa structure. Figures 10(e) and 10(f) are photographs of the packaged chip that is ready to be characterized. The protrusion of 2 μm is shown in Fig. 11(a). Although we have designed square protrusions of 2 μm, the corners are rounded. The reason is that the square corners of the photomask, which are illustrated in Fig. 11(b) (digital microscope, Keyence), are also rounded because of the photomask fabrication resolution. The experimental setup for measuring the device operation is illustrated in Fig. 12. This setup consists of three main evaluation apparatuses. (1) The first is a metallographic microscope (BM-3400TTRL, Wraymer) where a high-resolution digital camera (WRAYCAM-NOA200, Wraymer) is coupled to clearly visualize and take high-quality videos of the device operation. It is equipped with 5-, 10-, 20-, 40-, 100-fold magnification objective

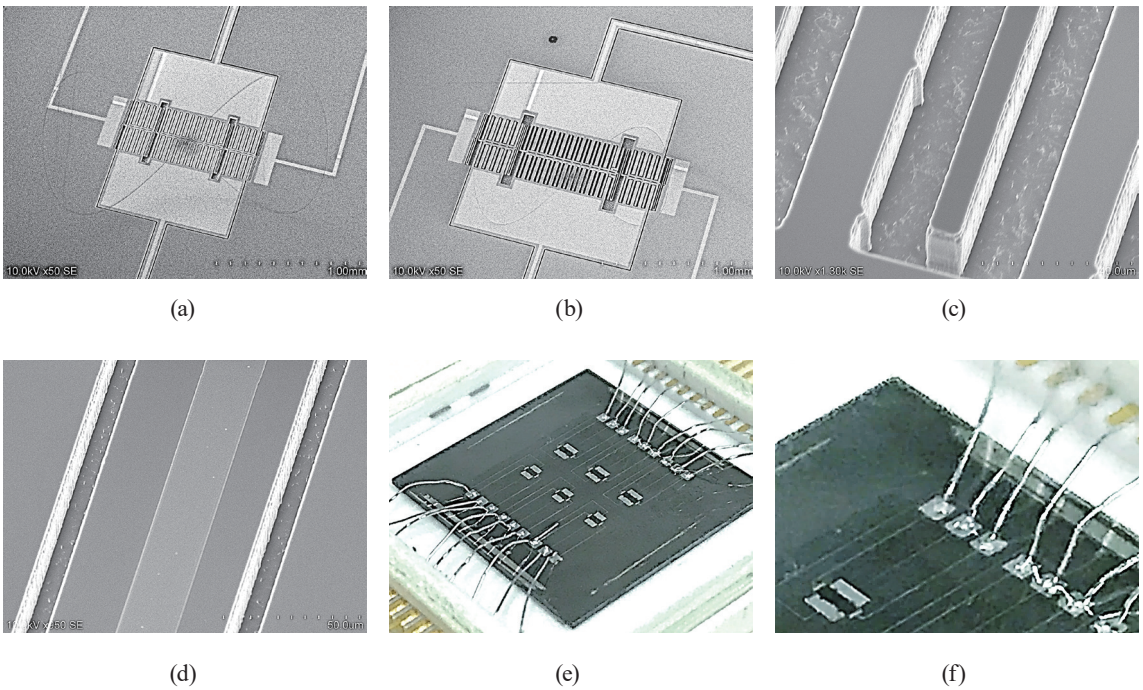

Fig. 10. (Color online) Fabricated device: (a) SEM image of design type-1 actuator, (b) SEM image of design type-2 actuator, (c) SEM image of interdigitated comb teeth, (d) SEM image of a mesa structure sandwiched by 10-μm-wide trenches, (e) photograph of packaged chip, and (f) enlarged image of (e).

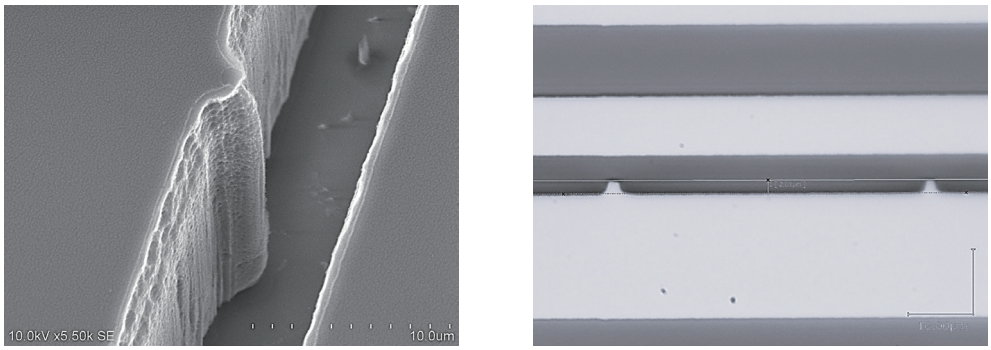

(a) (b)

Fig. 11. (Color online) Protrusion: (a) SEM image of protrusion and (b) microscopy image of photomask.

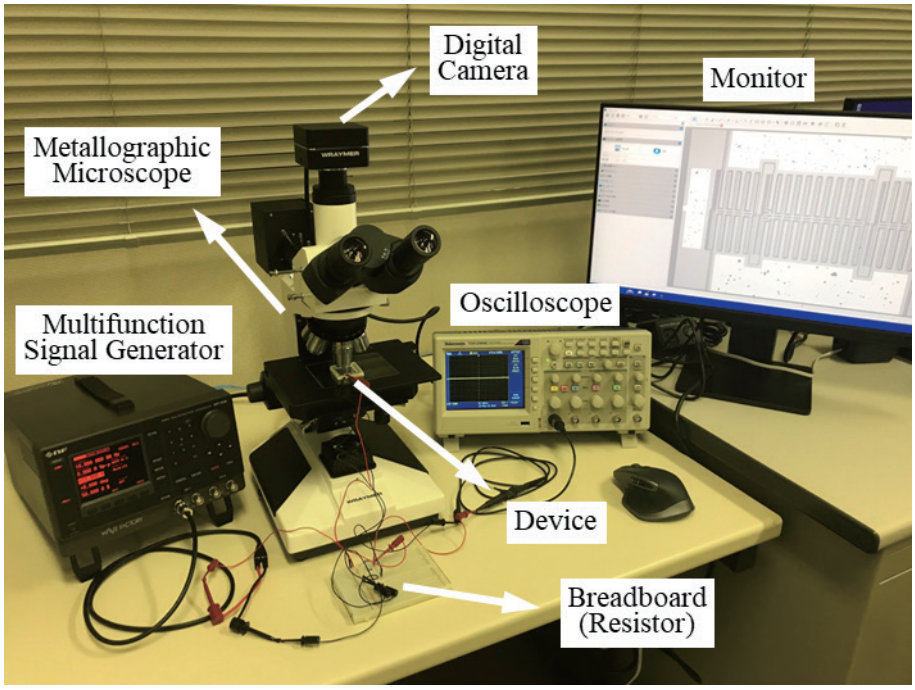

Fig. 12. (Color online) Experimental setup for device characterization.

lenses (GLF-PLACH#XLM, where # is the magnification, e.g., GLF-PLACH100XLM is a 100-fold magnification lens, Wraymer), so that one can verify the device from the entire structure to the detailed parts. (2) The second is a multifunction signal generator (WF1948, NF) that outputs a driving voltage to the device. (3) The third is a digital oscilloscope (TDS2004C, Tektronix) that monitors the driving voltage applied to the device. The driving voltage should be monitored owing to the use of a resistor with high resistance values. A 100 MΩ resistor has been used for short circuit protection, as mentioned in the structure concept subsection, and we verified relatively high thermal noise[28] on the driving voltage even when current is not flowing. When

movable comb teeth come into contact with the protrusions, contact resistance might occur, although we did not measure it quantitatively. Therefore, an external resistor on the order of 1 to 10 kΩ can be safely used. In this sense, we used a resistor with a resistance of 10 kΩ. Even if the contact resistance is zero, this resistor limits the current to only 1 mA, so that it would not damage the multifunction signal generator. The connection between the function generator and the lead of the package is made through a resistor installed on a breadboard.

Drive operation experiments have been video-recorded using the experimental setup mentioned above. The pictures shown in Fig. 13 have been captured from this video. We have characterized the device that corresponds to design type-1, as shown in Table 2 of Sect. 2.3. The device has been operated at a minimum dc voltage of 7.8 V. Figure 13(a) shows the entire device, while the set of three figures, i.e., Figs. 13(b), 13(c), and 13(d) show the enlarged areas for proof masses 1, 2, and 3, respectively. In the same manner, the set of (e), (f), and (g), the set of (h), (i), and (j), the set of (k), (l), and (m), and finally the set of (n), (o), and (p) also show the enlarged areas for these three proof masses. In each figure, among the three movable comb fingers, red dashed lines (color online) have been drawn on both edges along the length of the movable comb finger located on the left side of the figure for referring to the initial state. In the same manner, the yellow dashed lines (color online) are the reference lines for the pull-in state. The device operation is described as follows. (b)–(d) Initial state where no voltage is applied. (e)–(g) A driving voltage of 7.8 V has been applied, and then an afterimage of proof masses moving towards the fixed electrodes have been captured by the digital camera. (h)–(j) All proof masses are completely pulled in. (k)–(m) Driving voltage is completely taken away, and an afterimage of proof masses moving towards the initial position has been captured by the digital camera. (n)–(p) The proof masses returned to the initial state.

The experimental voltage is larger than the designed one. We have investigated the reason why a voltage of 7.8 V was necessary to pull in all the proof masses as follows. First we found the pull-in voltage for proof masses 1 and 3, which were experimentally pulled in at the same time at a voltage of 6.0 V, as shown in Fig. 14. Second, we measured the spring width and comb gaps, which sensitively affect the pull-in voltage value. Table 4 summarizes the dimensions of these parameters. As described in Sect. 2.3, the designed values are used for the photomask design. The gap values for the center proof mass are considered after the pull-in of the external proof mass.

Based on values in Table 4, the calculated pull-in voltage of the designed device for the external proof masses is 4.89 V, as shown in Table 5. For the fabricated device, the theoretically calculated and experimentally measured pull-in voltages are 5.86 and 6.0 V, respectively, and the relative error is about 2.3%. The discrepancies in the pull-in voltages between the designed and fabricated devices are due to the difference between expected and measured values. On the other hand, the "calculated pull-in voltage of the fabricated device" is more realistic for comparing the experimentally measured pull-in voltage, since it has been calculated based on measured values of the fabricated device. The calculation method is based on Eqs. (17), (18), and (22). The designed and experimentally measured pull-in distance, which corresponds to the total displacement from the initial to pull-in states, is 3.0 and 3.2 μm, respectively. From these results, one can say that the theoretical and experimental results are both rigorous and self-consistent.

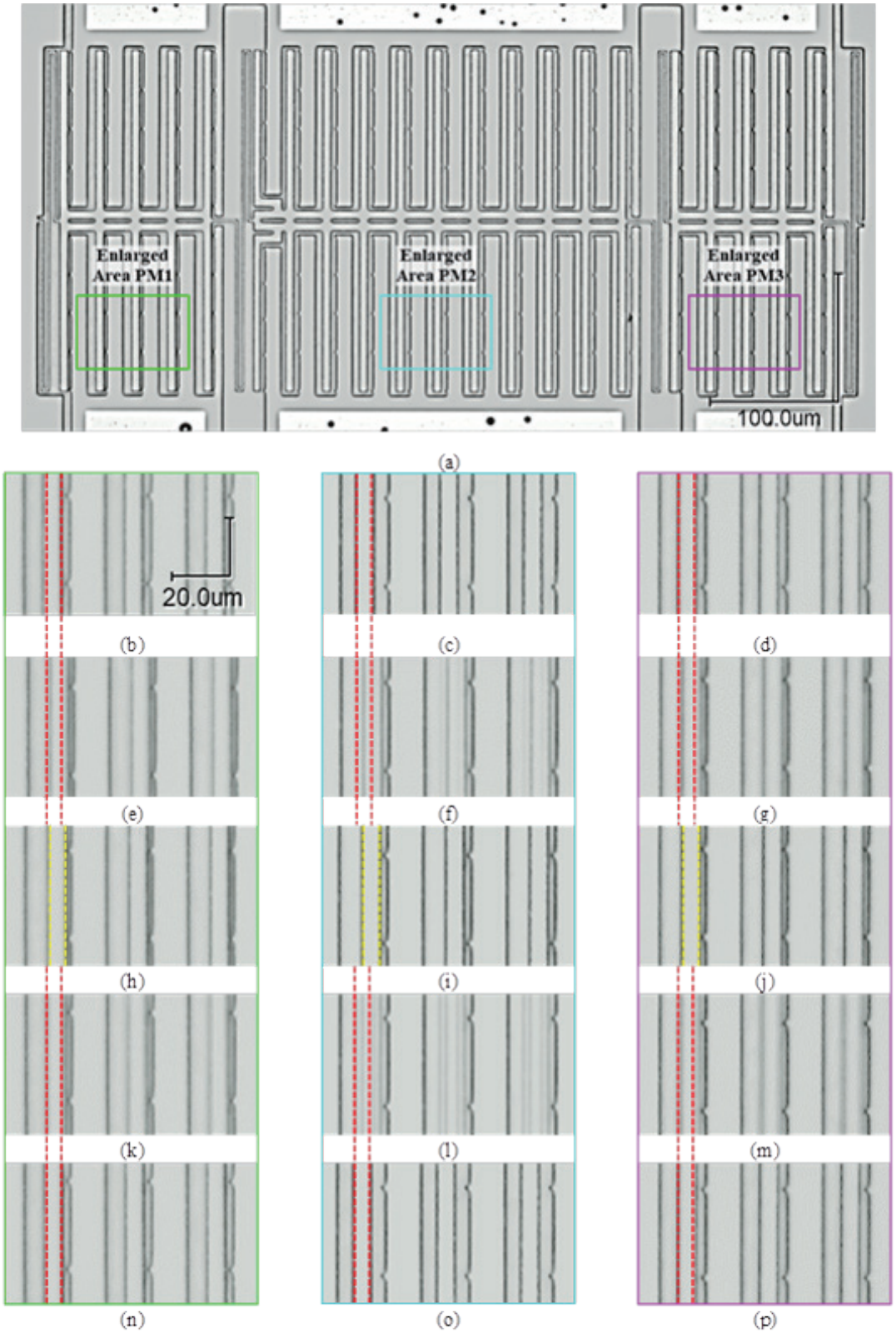

Fig. 13. (Color online) Device operation: (a) initial state (entire device view), (b)–(d) initial state [enlarged view of (a)], (e)–(g) afterimage of proof masses moving towards the fixed electrodes, (h)–(j) all proof masses are completely pulled in, (k)–(m) afterimage of proof masses moving towards the initial position, and (n)–(p) back to the initial condition. Red and yellow dashed lines are reference lines for initial and pull-in states, respectively.

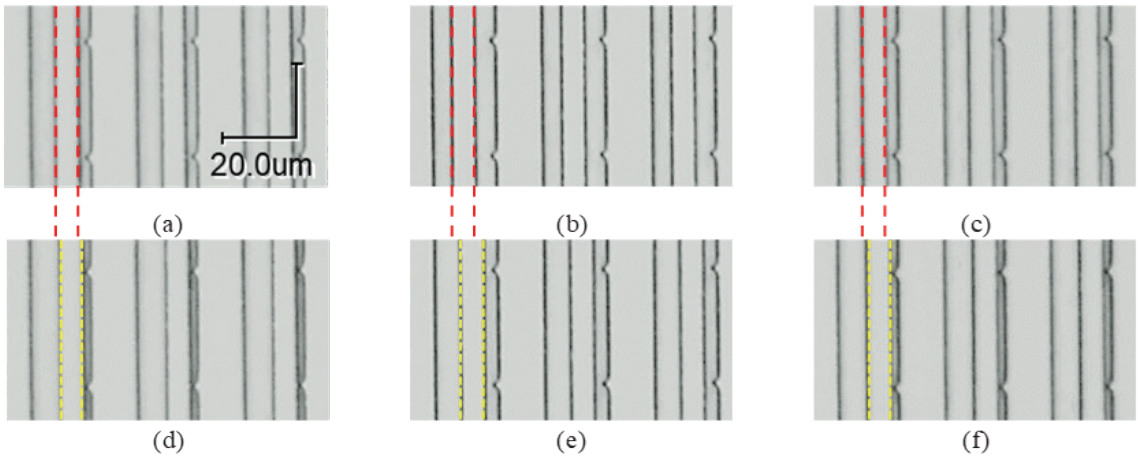

Fig. 14. (Color online) Device operation: (a)–(c) initial state, (d)–(f) when a voltage of 6.0 V is applied, the external proof masses (d) and (f) are pulled in, while the center proof mass (e) stops at a certain equilibrium state. Red and yellow dashed lines are reference lines for driving voltages of 0 V (no voltage is applied) and 6.0 V, respectively.

Table 4
Designed, expected (taking into account the half-width thinning or thickening of 250 nm after fabricating the device, as described in Sect. 2.1), and measured values. The parameters are defined in Fig. 7(b).

	Designed	Expected	Measured
Spring width (μm)	2.5	2.0	2.2
g_{EXT} (g_R) (μm)	5.0	5.5	5.2
$g_{EXT\ OPP}$ (g_L) (μm)	10.0	10.5	9.0
g_{CTR} (g_R) (μm)	5.0	5.0	6.2
$g_{CTR\ OPP}$ (g_L) (μm)	11.0	11.0	9.1

Table 5
Calculated and measured pull-in voltages, and pull-in distance (total displacement from the initial state) of the external proof mass for designed and fabricated devices.

	Designed	Fabricated
Calculated pull-in voltage (V)	4.89	5.86
Measured pull-in voltage (V)	—	6.0
Pull-in distance (μm)	3.0	3.2

On the other hand, we verified that the gaps of the center proof mass for the "expected" and "fabricated" devices differ from 18 to 24%, after the pull-in of the external proof masses. Theoretically, the pull-in voltage of the center proof mass is 4.40 V after pulling in the external proof masses at a voltage of 5.0 V, which means that the pull-in phenomenon for all external and center proof masses should occur instantaneously when a driving voltage of 5.0 V is applied. The

same should occur for the fabricated device, although the measured pull-in voltage is 6.0 V. However, the center proof mass stops at a certain equilibrium state, as verified in Fig. 14(e). In this state, the measured gaps are g_{CTR} = 6.2 μm and $g_{CTR\ OPP}$ = 9.1 μm, as shown in Table 4. The calculated pull-in voltage of 7.68 V has been obtained using these values with Eqs. (17), (18), and (22). Since the experimentally measured pull-in voltage is 7.8 V, the relative error is about 1.5%. Moreover, we have verified that the initial gaps of the interdigitated comb teeth of the center mass are symmetrical, i.e., gap g_{CTR} is equal to gap $g_{CTR\ OPP}$, as can be seen in Table 2; thus, the forces are balanced. This is the reason why a voltage higher than the designed one is needed to pull in the center proof mass. As the left proof mass moves, a pushing force is transferred from the spring connected to the center proof mass, and the force balance is lost. At the same time, a pulling force is transferred from the spring that connects the right and center proof masses also causing a force balance loss. However, since the forces are initially balanced, the resultant force is not enough to pull in the center proof mass. Therefore, to ensure a pull-in of the center proof mass, the force generated between electrode combs with gap g_{CTR} must be much higher than the force generated between electrodes with gap $g_{EXT\ OPP}$. As a result, higher voltage will be necessary to pull-in the center proof mass. Table 6 summarizes the calculated and measured values of the pull-in voltages for the fabricated actuator. As can be seen, good agreement between theoretical and experimental results are obtained.

If the initial gap $g_{EXT\ OPP}$ is about twice larger than the gap g_{CTR}, one can obtain a lower pull-in voltage. For example, let us calculate the pull-in voltage of the designed actuator based on the expected dimension. After the external proof masses are pulled-in by an amount of 3.0 μm at a voltage of 4.89 V, the gaps for g_{CTR} and g_{CTR} are 5.5 and 20 μm, respectively. Thus, we obtain a theoretical pull-in voltage of 4.55 V for the center proof mass. Since the pull-in voltage for the center proof mass is slightly smaller than to that of the external proof masses, when a voltage of 4.89 V is applied to the actuator, all the proof masses will pull-in and they will instantaneously come into contact with the fixed electrodes. Thus, the total displacement of the actuator will be 6.0 μm, as expected.

Table 7 shows the results of other research that claim large displacement at low dc driving voltage. To make a reasonable comparison, the driving voltage denoted in the table is for a displacement of 6 μm, as long they are available from theoretical or experimental graphs in the literature. We have selected representative research over two decades [2003–2023 (at present)].

Clearly, for the same amount of displacement, we have achieved the smallest driving voltage in comparison to other studies.

Table 6
Calculated and measured pull-in voltages, for the external proof masses and center mass for the fabricated actuator.

	External proof masses	Center proof mass
Calculated pull-in voltage (V)	5.86	7.68
Measured pull-in voltage (V)	6.0	7.8
Relative error (%)	2.3	1.5

Table 7
Actuators having large displacement at low dc driving voltage.

Refs.	Year	Device type	Driving Voltage (V)	Disp. (μm)	Data type
This study	2023	Combination of parallel plate and comb drive actuators with proof mass suspended by springs	4.89	6	Theory
			7.8	6	Experiment
14	2023	Parallel plate with proof mass suspended by springs	35	6	Experiment
15	2023	Cantilever	17	3	Theory
16	2022	Parallel plate with proof mass suspended by springs	40	6	Experiment
17	2021	Parallel plate with proof mass suspended by springs	85	6	Experiment
18	2020	Diaphragm	12.5	5	Theory
19	2019	Combination of cantilever and comb drive actuator	12	6	Theory
20	2017	Parallel plate with proof mass suspended by springs	12	6	Theory
21	2012	Comb drive actuator with proof mass suspended by springs	30	6	Experiment
22	2006	Combination of parallel plate and comb drive actuators with proof mass suspended by springs	56	4	Theory
23	2003	Comb drive actuator with proof mass suspended by springs	36	6	Experiment

4. Conclusions

As a current trend in the MEMS field, the demand for controlling MEMS devices by using LSI and MCU boards that operate at low voltage is significantly increasing. However, no microactuator capable of outputting a large displacement at such a low driving voltage has yet been developed, which is still a major unsolved problem. In this study, we have revealed that the driving voltage can be considerably reduced by setting the interdigitated comb teeth gaps at the pull-in stability threshold for a comb drive actuator consisting of conjoined proof masses connected to each other by serpentine springs.

In the theoretical model, we derived for the first time, analytical equations for the displacement as functions of voltage, the pull-in voltage and pull-in displacement as well for interdigitated comb drive actuators. These are significant achievements, since prior researches has only yielded the electrostatic force equation or only the pull-in voltage and pull-in distance for simple parallel-plate electrodes. Moreover, using these equations, we revealed that the relative error between theoretical and experimental voltages is about 2%. This is a very promising result, since no sophisticated software is necessary to design a comb drive actuator.

Based on the novel actuator concept, a voltage of 4.89 V, which is lower than the maximum operation voltage of LSI and MCU boards, has been theoretically obtained to move all the proof masses for a displacement of $\Delta d = 6$ μm. The actuator has been fabricated, and to move the same distance Δd, we have experimentally obtained a voltage of 7.8V. The reason for such a difference lies in the designed value of the initial gap between the interdigitated comb teeth of the center proof mass. Nevertheless, both theoretical and experimental values are less than 10 V, which are lower than in any other representative reports picked up by the author over these two decades that claim low driving voltage for high displacement. Clearly, only this study yielded single-digit driving voltage, which means that we achieved a state-of-the-art electrostatic microactuator. The impact of this result in the MEMS field is very significant, since MEMS actuators controlled by

LSI and MCU boards will lead to future applications that need high performance controllability and functionality.

Acknowledgments

This work was supported by JSPS KAKENHI Grant Number 18K04913. A part of this work was conducted at Tohoku University, supported by the "Nanotechnology Platform Program" of the Ministry of Education, Culture, Sports, Science and Technology (MEXT), Japan, Grant Number JPMXP09F21TU0079.

References

1 M. Esashi and S. Tanaka: Jpn. Inst. Electron. Packag. **24** (2017) 6 (in Japanese). https://doi.org/10.5104/jiep.20.372
2 M. Esashi and S. Tanaka: Micromachines **7** (2016) 8. https://doi.org/10.3390/mi7080137
3 M. Esashi and S. Tanaka: Micro Nano Syst. Lett. **1** (2013) 3. https://doi.org/10.1186/2213-9621-1-3
4 M. Esashi: Jpn. J. Appl. Phys. **51** (2012) 8R. https://doi.org/10.1143/JJAP.51.080001
5 Arduino.CC: https://www.arduino.cc/ (accessed March 2023).
6 K. Yamaguchi, K. Katsura, T. Yamada, and Y. Sato: IEEJ Open J. Ind. Appl. **7** (2018) 3. https://doi.org/10.1541/ieejjia.7.218
7 C. Li, K. Tan, B. Ji, Z. Wang. S. Ding, and P. Lefley: IET Power Electron. **15** (2022). https://doi.org/10.1049/pel2.12248
8 S. Wang, X. Ding, and Q. Tan: J. Sens. **2022** (2022). https://doi.org/10.1155/2022/7834718
9 X. Guo, Q. Xun, Z. Li, and S. Du: Micromachines **10** (2019) 6. https://doi.org/10.3390/mi10060406
10 S. H. Chung, S. K. Lee, C. H. Ji, and J. H. Park: Sens. Actuators, A **290** (2019) 1. https://doi.org/10.1016/j.sna.2019.03.021
11 H. M. Chu, J. Mizuno, and K. Hane: J. Vac. Sci. Technol. B **29** (2011) 4. https://doi.org/10.1116/1.3605301
12 H. M. Chu and K. Hane: Sens. Actuators, A **165** (2011) 2. https://doi.org/10.1016/j.sna.2010.11.004
13 H. M. Chu, T. Tokuda, M. Kimata, and K. Hane: J. Microelectromech. Syst. **19** (2010) 4. https://doi.org/10.1109/JMEMS.2010.2055545
14 M. Allameh, Y. Zhou, D. Chrusch, B. Park, and C. Shafai: J. Micromech. Microeng. **33** (2023) 034008. https://doi.org/10.1088/1361-6439/acb956
15 X. Yang, P. Kästner, E. Käkel, M. Smolarczyk, S. Liu, Q. Li, and H. Hillmer: App. Sci. **13** (2023) 1118. https://doi.org/10.3390/app13021118
16 K. Kim, Y. Lee, I. L. Garro, and J. M. Kim: Sensors **22** (2022) 9490. https://doi.org/10.3390/s22239490
17 D. Admassu, T. Durowade, S. Velicu, S. Sivananthan, and W. Gao: Microsyst. Technol. **27** (2021) 2751. https://doi.org/10.1007/s00542-020-05022-1
18 A. C. Atik, M. D. Özkan, E. Özgur, H. Külah, and E. Yıldırım: J. Micromech. Microeng. **30** (2020) 115001. https://doi.org/10.1088/1361-6439/aba16f
19 W. Bian, J. Zhao, and Z. You: J. Micromech. Microeng. **29** (2019) 065014. https://doi.org/10.1088/1361-6439/ab1635
20 C. Li, R. N. Dean, and G. T. Flowers: Microsyst. Technol. **23** (2017) 1125. https://doi.org/10.1007/s00542-016-2903-6
21 C. M. Chang, S. Y. Wang, R. Chen, J. A. Yeh, and M. T. Hou: Sensors **12** (2012) 10881. https://doi.org/10.3390/s120810881
22 S. Kamide and K. Suzuki: IEEJ Trans. Sns. Micromech. **126** (2006) 453. https://doi.org/10.1541/ieejsmas.126.453
23 J. D. Grade, H. Jerman, and T. W. Kenny: J. Microelectromech. Syst. **12** (2003) 335. https://doi.org/10.1109/JMEMS.2003.811750
24 M. Lishchynska, N. Cordero, O. Slattery, and C. O'Mahony: Sens. Lett. **4** (2006) 200. https://doi.org/10.1166/sl.2006.011
25 M. Bao: Analysis and Design Principles of MEMS Devices (Elsevier B. V., Amsterdam, 2005) 1st ed., Chap.4. https://doi.org/10.1016/B978-0-444-51616-9.X5000-0

26 G. Barillaro, A. Molfesee, A. Nannini, and F. Pieri: J. Micromech. Microeng. **15** (2005) 736. https://doi.org/10.1088/0960-1317/15/4/010
27 W. I. Jang, C. A. Choi, M. L. Lee, C. H. Jun, and Y. T. Kim: J. Micromech. Microeng. **12** (2002) 3. https://doi.org/10.1088/0960-1317/12/3/316
28 D. Walter, A. Bulau, and A. Zimmermann: Sensors **23** (2023) 1107. https://doi.org/10.3390/s23031107

About the Author

Jun Mizuno received his B.E. degree from Sao Paulo University, Brazil, in 1994 and his M.E. and Dr. Eng. degrees from Tokyo Institute of Technology, Japan, in 1996 and 1999, respectively. From 2012 to 2015, he was an associate professor at Ishinomaki Senshu University, Japan. Since 2016, he has been a professor at the same university. His research interests are in MEMS and robotic systems. (mizuno@isenshu-u.ac.jp)